

## Modeling and Analysis of Nonlinear Chaotic Mechanical Dynamics in Laser Scanning Systems

José A. Núñez-López <sup>1</sup>, David Meza-García <sup>2</sup>, Oleg Sergiyenko <sup>3</sup>, Vera Tyrsa <sup>4</sup>, Julio C. Rodríguez-Quiñonez <sup>5</sup>, Wendy Flores-Fuentes <sup>6</sup>, Fernando Lopez-Medina <sup>7</sup>, Cesar Sepulveda-Valdez <sup>8</sup>, J. Fabián Villa-Manriquez <sup>9</sup>, Humberto Andrade-Collazo <sup>10</sup>, Evgeny Burnaev <sup>11</sup>, Svetlana Illarionova <sup>12</sup>, Danilo Cáceres- Hernández <sup>13</sup> and Ruben Alaniz-Plata <sup>14</sup>

<sup>1</sup>Engineering Institute, Autonomous University of Baja California, Mexicali, Mexico, <sup>2</sup>Engineering Faculty, Autonomous University of Baja California, Mexicali, Mexico, <sup>3</sup>Skolkovo Institute of Science and Technology (Skoltech), Moscow, Russia, <sup>4</sup>Intelligent Systems Laboratory, Faculty of Electrical Engineering, Technological University of Panama, Panama.

**ABSTRACT** This paper presents a novel approach to modeling and analyzing chaotic mechanical vibrations in laser scanning systems. The model explicitly incorporates nonlinear friction using the LuGre friction model. Experimental validation demonstrates chaotic behavior manifested in irregular velocity fluctuations. Dominant frequencies and maximum vibration amplitudes were identified under various operational conditions. A maximum disturbance amplitude of 1.65 rad/s<sup>2</sup> was observed under the most demanding conditions (25 RPS, ±15° inclination). The proposed model was validated experimentally, providing insights into the interplay of chaotic vibrations and nonlinear friction. A robust control strategy was introduced to mitigate these effects. This strategy is supported by Lyapunov stability analysis and computational implementation. The results demonstrate the effectiveness of the control strategy in reducing the negative effects of friction and chaotic vibrations. The findings could benefit precision engineering, nonlinear dynamics research, and machine vision.

**KEYWORDS**  
Chaos theory  
Nonlinear dynamics  
Friction  
Vibrations  
Laser scanning

### INTRODUCTION

Laser scanners are essential tools in industry, providing precise distance mapping and high-speed image processing capabilities. These systems are widely applied in tasks such as accurate measurements, part identification, and robotic control (Sergiyenko *et al.*

2020). An example is the Technical Vision System (TVS), described in (Lindner 2021), which integrates a laser scanning system utilizing the Dynamic Triangulation measurement method to calculate 3D coordinates within its field of view (FOV). The system employs electric motors to drive both the positioning laser (PL) and the scanning aperture (SA), enabling mapping across the FOV.

Friction is a complex and nonlinear phenomenon arising from the contact between surfaces, significantly affecting the positioning accuracy of mechanical systems (Gohar and Rahnejat 2012). Various models have been proposed over time to describe friction, each with its limitations in capturing all its effects (Canudas de Wit *et al.* 1995; Armstrong-Hélouvy *et al.* 1994; Popov *et al.* 2010). Understanding friction is crucial for designing control laws to mitigate its undesirable effects (Selivanov and Fridman 2023; Marton and Lantos 2007). Friction can be modeled as static or dynamic and is described using algebraic or differential equations (Armstrong-Hélouvy *et al.* 1994).

On the other hand, mechanical vibrations are a nonlinear and complex consequence of motion in mechanical systems (Lazutkin *et al.* 2017). These phenomena can arise from various sources, such as unbalanced forces, external excitations, or interactions be-

**Manuscript received:** 12 January 2025,

**Revised:** 18 March 2025,

**Accepted:** 21 April 2025.

<sup>1</sup>jose.nunez10@uabc.edu.mx

<sup>2</sup>david.meza.garcia@uabc.edu.mx (Corresponding author)

<sup>3</sup>srgnk@uabc.edu.mx

<sup>4</sup>vtysa@uabc.edu.mx

<sup>5</sup>julio.rodriguez81@uabc.edu.mx

<sup>6</sup>flores.wendy@uabc.edu.mx

<sup>7</sup>fernando.lopez.medina@uabc.edu.mx

<sup>8</sup>cesar.sepulveda@uabc.edu.mx

<sup>9</sup>fabian.manriquez@uabc.edu.mx

<sup>10</sup>humberto.andrade@uabc.edu.mx

<sup>11</sup>e.burnaev@skoltech.ru

<sup>12</sup>s.illarionova@skoltech.ru

<sup>13</sup>danilo.caceres@utp.ac.pa

<sup>14</sup>ruben.alaniz@uabc.edu.mx

tween components, and they significantly impact the stability and precision of positioning systems. Vibrations can exhibit chaotic behavior under certain conditions, further complicating their analysis and control (Zhao *et al.* 2010). While studies on nonlinear vibrations in cantilever beams and structural systems have provided insights into how stiffness and damping variations influence dynamic response (Pany and Rao 2004; Pany 2023; Pany and Rao 2002), in laser scanning systems, such vibrations, coupled with friction effects, can degrade the accuracy of the scanning process rather than geometric anisotropies, leading to errors in positioning and measurement (Liu *et al.* 2021).

This paper focuses on modeling and estimating the chaotic vibrations observed in laser scanning systems, specifically those influenced by frictional forces. By leveraging experimental data from MPU6050 vibration sensors and the open-loop response of the scanning aperture system, authors propose a comprehensive approach to analyze and mitigate these effects. The developed model and its validation through numerical simulations and physical experimentations aim to provide a robust tool for understanding and controlling the intricate dynamics of mechanical vibrations in these applications.

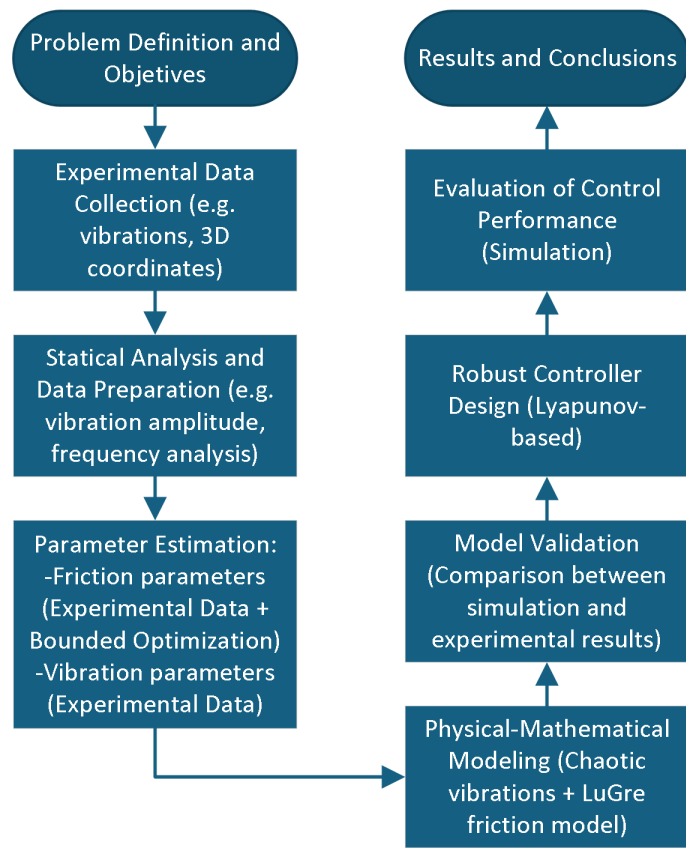


**Figure 1** Overall methodology flow chart describing key stages of the research.

The novelty of this research lies in the explicit modeling and control of nonlinear chaotic vibrations coupled with frictional effects in laser scanning actuator subsystems, a topic scarcely addressed in current literature. While existing studies have explored nonlinear dynamics or friction individually, there remains a gap in simultaneously addressing chaotic vibrational disturbances combined with nonlinear friction in laser scanning actuator systems. This

paper specifically addresses this gap by integrating the experimental characterization of chaotic vibrations into a robust nonlinear control framework, validated by Lyapunov stability analysis and experimental data.

Figure 1 shows the overall methodology followed in this study, highlighting the integration of experimental measurements, statistical analysis, physical-mathematical modeling, parameter estimation, validation, and robust control design.

## TECHNICAL VISION SYSTEM

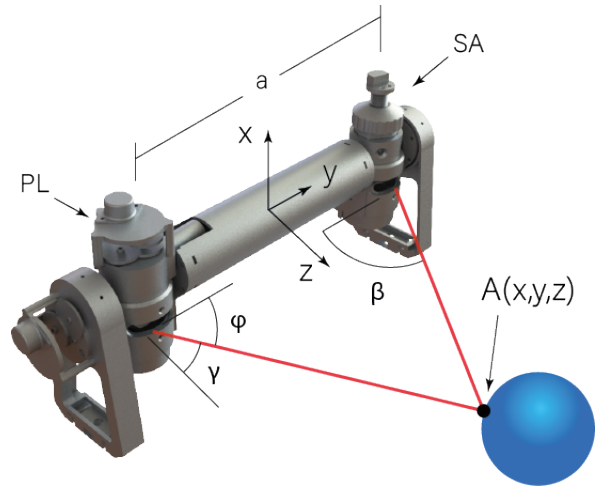


**Figure 2** Diagram of the Laser Scanner TVS prototype.

The TVS (Figure 2) prototype was fabricated using PLA plastic filament via 3D printing, selected due to its mechanical properties that are suitable for lightweight robotic applications. Studies have reported the following characteristics for PLA:

- **Yield Strength:** 45 MPa (Al Khawaja *et al.* 2020).
- **Hardness:** Ranging from 55 to 76.33 Shore D in non-planar models (Atef *et al.* 2022).
- **Natural Frequency:** Approximately 214 Hz (Kushwaha *et al.* 2022).

These mechanical properties influence the structural behavior of the TVS, particularly its response to vibrations, which may affect coordinate accuracy. Since this prototype can be integrated into mobile robots or mounted on an optical table, different mechanical constraints may alter its vibrational response (Sergiyenko *et al.* 2020; Sepulveda-Valdez *et al.* 2024; Alaniz-Plata *et al.* 2025).

### Dynamic Triangulation Method

The TVS operation is based on the dynamic triangulation method, which enables accurate three-dimensional mapping by combining angularly directed laser beams, reflective surface analysis, and geometric principles. The system is composed of two main subsystems: the Positioning Laser (PL) and the Scanning Aperture (SA). These components work together to capture and process the reflected light from obstacles, ultimately calculating the 3D coordinates of the reflection point with the following equations:

$$x = a \left( \frac{\sin(\varphi) \sin(\beta)}{\sin(\varphi + \beta)} \right) \quad (1)$$

$$y = a \left( \frac{1}{2} - \frac{\cos(\varphi) \sin(\beta)}{\sin(\varphi + \beta)} \right) \quad (2)$$

$$z = a \left( \frac{\cos(\varphi) \sin(\beta) \tan(\gamma)}{\sin(\varphi + \beta)} \right) \quad (3)$$

These equations allow determining a specific point in three-dimensional space ( $x, y, z$ ) based on the given parameters, such as the angle  $\varphi$ , the angle  $\beta$ , the angle  $\gamma$ , and the value of  $a$ . The parameter  $a$  represents the fixed baseline distance between the Positioning Laser (PL) and the Scanning Aperture (SA). By varying the angles  $\beta$  and  $\gamma$ , multiple points in space are generated, allowing for the visualization of a broader spatial distribution. This approach is particularly useful for analyzing trajectories, point distributions, or patterns generated by angular variations in three-dimensional systems.

### Positioning Laser

The Positioning Laser subsystem (Figure 3) is responsible for accurately directing a laser beam to various points within the environment. It is composed of four main components: a laser emitter, two 45-degree inclined mirrors—one fixed and one movable—and two stepper motors.

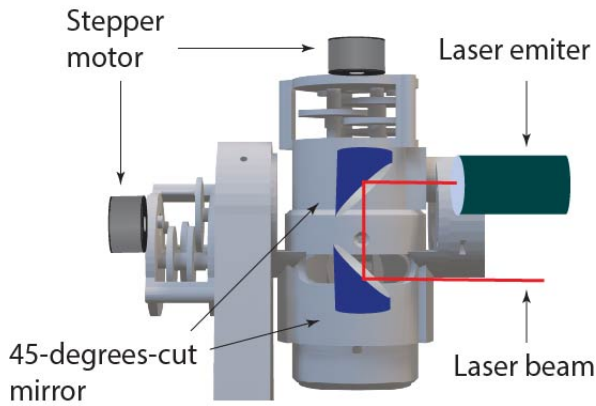


**Figure 3** Diagram of the Positioning laser (PL).

The operation begins with the laser emitter generating a laser beam, which is initially directed toward a fixed 45-degree inclined mirror. This mirror redirects the beam orthogonally toward a second rotating mirror. The rotating mirror, mounted on a movable axis, dynamically adjusts the direction of the laser beam with the aid of one of the stepper motors. This motor enables the mirror to be precisely oriented in small increments of angularity, controlling the angle  $\varphi$ .

Furthermore, the second stepper motor controls the movement of the main rod in the TVS, adjusting the angle  $\gamma$ . Together, these angles,  $\varphi$  and  $\gamma$ , determine the location of the laser beam within the FOV, allowing the subsystem to target specific points in the environment as needed.

### Scanning Aperture

The Scanning Aperture (Figure 4) is the main component of the TVS, designed to capture and process laser beams reflected off surfaces in the environment. Its key function is to determine the reflection angle, which is used to calculate the three-dimensional coordinates of the reflected points. This system includes a 45° rotating mirror that redirects the beams toward a lens array, which focuses the light onto an optical sensor. The Scanning Aperture subsystem integrates a DC motor as an actuator, which converts electrical energy into mechanical motion to rotate the 45° mirror.

This sensor detects the reflected beams and confirms the presence of obstacles, while a zero-position sensor synchronizes these detections with the angular position of the mirror, generating reference pulses during each 360° rotation. The incidence angle  $\beta$  is estimated using the pulses recorded by both sensors, allowing the integration of geometric and temporal information. This design, based on sensor synchronization and the dynamic control of the rotating mirror, ensures quasi-real-time measurements.

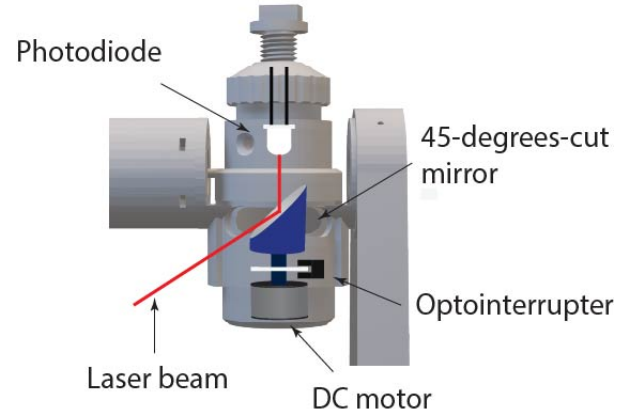


**Figure 4** Diagram of the Scanning aperture (SA) subsystem.

## MODEL DEVELOPMENT

To address the problem of scanning velocity stability in laser scanning systems, authors consider the dynamics of the DC motor responsible for the scanning aperture. The proposed model integrates both electrical and mechanical behaviors, incorporating the influence of friction and mechanical vibrations.

### General Dynamic Model

To address disturbances in the scanning process, the dynamics of the electric drive system can be generalized as:

$$\dot{x}(t) = Ax(t) + Bu(t) + C\rho(t) \quad (4)$$

$$y(t) = Dx(t) \quad (5)$$

where: In this formulation,  $x(t) \in \mathbb{R}^n$  is the state vector of dimension  $n$ , which includes variables such as angular position, velocity, and current. The control input vector of dimension  $m$  is denoted as  $u(t) \in \mathbb{R}^m$ , while the output vector of dimension  $l$ ,  $y(t) \in \mathbb{R}^l$ , represents measurable quantities like the scanning velocity or position. The matrices  $A$ ,  $B$ ,  $C$ , and  $D$  define the system dynamics and coupling terms. The term  $\rho(t) \in \mathbb{R}^p$  accounts for external disturbances vector of dimension  $p$ , which are assumed to be unknown but bounded. This general description provides the base for analyzing faults and disturbances in the scanning aperture system, enabling robust control.

### DC Motor Model

The DC motor drives the scanning aperture and is modeled by the following state-space representation, derived from its electrical and mechanical characteristics:

$$\dot{x}_1(t) = x_2(t) \quad (6)$$

$$\dot{x}_2(t) = -\frac{k_v}{J}x_2(t) + \frac{k_M}{J}x_3(t) \quad (7)$$

$$\dot{x}_3(t) = -\frac{k_b}{L}x_2(t) - \frac{R}{L}x_3(t) + \frac{k_u}{L}u(t) \quad (8)$$

In this model,  $x_1(t)$  represents the angular position of the motor output shaft, while  $x_2(t)$  denotes the angular velocity at the same point. The variable  $x_3(t)$  corresponds to the current flowing through the motor windings, and  $u(t)$  represents the input voltage applied to the motor. The parameter  $J$  is the combined moment of inertia of the motor and the scanning aperture assembly, which characterizes the system's resistance to changes in rotational speed. The term  $k_v$  is the viscous friction coefficient, reflecting the losses due to mechanical friction, and  $k_M$  is the torque constant, which relates the motor's torque to the current. The back electromotive force (EMF) constant,  $k_b$ , links the angular velocity to the induced voltage in the motor windings. Additionally,  $R$  and  $L$  are the armature resistance and inductance, respectively, defining the electrical dynamics of the motor, while  $k_u$  represents the amplification factor of the input voltage.

### Incorporating Nonlinear Effects of Vibrations and Friction

Friction and mechanical vibrations are integral to the system dynamics. Vibrations are modeled as a nonlinear perturbation, potentially exhibiting chaotic behavior, which couples with frictional forces in the following manner:

It is assumed that the motor is influenced by mechanical vibrations, which lead to variations in the velocity of the motor output shaft. These variations, caused by the vibrational disturbances, can be introduced into the model (4) through an unknown function  $\Delta_v(t)$ , resulting in the following system of equations:

$$\dot{x}_1(t) = x_2(t) \quad (9)$$

$$\dot{x}_2(t) = -\lambda_1 x_2(t) + \lambda_2 x_3(t) - \lambda_3 \tau_f(t) - \Delta_v(t) \quad (10)$$

$$\dot{x}_3(t) = -\lambda_4 x_2(t) - \lambda_5 x_3(t) + \lambda_6 u(t) \quad (11)$$

Table 1 presents the mathematical expressions used to define the system parameters  $\lambda_1$  to  $\lambda_6$ . The numerical values of the physical parameters involved in these expressions were provided in the 'Characterization and Parameter Estimation' subsection.

■ **Table 1** Mathematical Expressions for System Parameters

Parameter	Mathematical Expression
$\lambda_1$	$k_v/J$
$\lambda_2$	$k_M/J$
$\lambda_3$	$1/J$
$\lambda_4$	$k_b/L$
$\lambda_5$	$R/L$
$\lambda_6$	$k_u/L$

where:

- $\tau_f(t)$ : Nonlinear frictional torque, modeled as a nonlinear function of velocity and position.

- $\Delta_v(t)$ : Perturbation due to mechanical vibrations, derived from experimental data using the MPU6050 sensor.

In this model of the laser scanning system, the function  $\Delta_v(t)$  represents the influence of mechanical vibrations, which affects the stability of the electric drive's rotation speed. This instability directly impacts the accuracy of the scanning process. The main objective of the research is to estimate  $\Delta_v(t)$  and, if its value exceeds a predefined threshold, to account for it in signal processing to estimate the effects of vibrational disturbances on system performance. These vibrations are inherently random, as captured experimentally using the MPU6050 sensor. Therefore, authors model  $\Delta_v(t)$  as:

$$\Delta_v(t) \approx \sigma_v dW(t), \quad (12)$$

where:

- $\sigma_v$ : The amplitude of the stochastic noise, estimated experimentally as the standard deviation of the captured data.
- $dW(t)$ : The increment of a Wiener process, representing the random nature of the vibrational disturbances.

In practice, the experimentally captured data serves as a direct approximation of  $\Delta_v(t)$ , capturing both the amplitude and the randomness of the mechanical vibrations (Kumičák 2004; Banerjee 2021). Therefore, the vibrations measured at the motor base, transmitted to the shaft, induce an additional torque in the mechanical dynamics. Using the experimentally obtained angular acceleration of the vibration, this disturbance torque can be represented as:

$$\tau_v = J\Delta_v(t) \quad (13)$$

where  $\tau_v$  is the combined moment of inertia of the motor and the scanning aperture assembly. The modeled vibration term  $\tau_v$  is subject to the upper bound:

$$|\tau_v| \leq \tau_v^{max} \quad (14)$$

where the value  $\tau_v^{max} = J\Delta_v^{max}$  denotes the maximum positive value of the modeled vibration torque.

The LuGre friction model, originally proposed in (Canudas de Wit et al. 1995), provides an effective framework for approximating the nonlinear dynamics of friction. It assumes the presence of micro-imperfections on the contact surfaces, which are modeled as bristle-like deflections to represent the distributed deformation of asperities. While these micro-imperfections are not directly measured, their existence is inferred and incorporated into the model as a deterministic approximation. This approach has been widely adopted in various applications, including DC motor systems (Núñez-López et al. 2023; Wang et al. 2016; Freidovich et al. 2009).

The nonlinear friction torque is described by:

$$\tau_f(\omega) = \sigma_0 \left( 1 - \sigma_1 \frac{|\omega|}{g(\omega)} \right) z \quad (15)$$

In this equation, the internal variable  $z$  represents the average deflection of the bristle-like elements at the contact surface. The parameter  $\sigma_0$  corresponds to the bristle stiffness coefficient, encapsulating the elastic behavior of the asperities, while  $\sigma_1$  reflects the bristle damping coefficient, accounting for energy dissipation during frictional interactions (Canudas de Wit et al. 1995).

The transition from static to dynamic friction, a phenomenon critical to capturing real-world behavior, is modeled through the Stribeck effect (Na et al. 2018). This is expressed as:

$$g(\omega) = \tau_c + (\tau_s - \tau_c)e^{-(\omega/v_0)^2} \quad (16)$$

Here,  $\tau_c$  denotes the Coulomb friction torque, which is independent of velocity, while  $\tau_s$  represents the stiction torque, describing the peak force required to overcome static friction. The parameter  $v_0$  defines the Stribeck velocity threshold.

The LuGre friction model ensures symmetry about the origin (Canudas de Wit et al. 1995) and permits adhering to the following upper bound:

$$|\tau_f(\omega)| \leq \tau_s \quad (17)$$

where  $\tau_s$  represents the maximum static friction torque, serving as an upper limit for the nonlinear frictional behavior. In previous studies (Wang et al. 2016; Freidovich et al. 2009), this model has been parameterized to suit various applications, highlighting its adaptability in DC motor systems.

Based on experimental data and a review of relevant literature, the authors consider this formulation to provide a reliable theoretical framework. The subsequent section will present the model validation for the specific system under study.

### MODEL VALIDATION AND REAL-TIME MEASUREMENT OF VIBRATIONS IN THE TVS LASER SCANNING

Experimental validation of the proposed model was performed using the open-loop response and data from MPU6050 vibration sensors, installed on the aperture and positioner (see Fig.5) of the laser scanning system. The results demonstrate the model's capability to accurately predict the dynamics of the scanning system under various operating conditions.

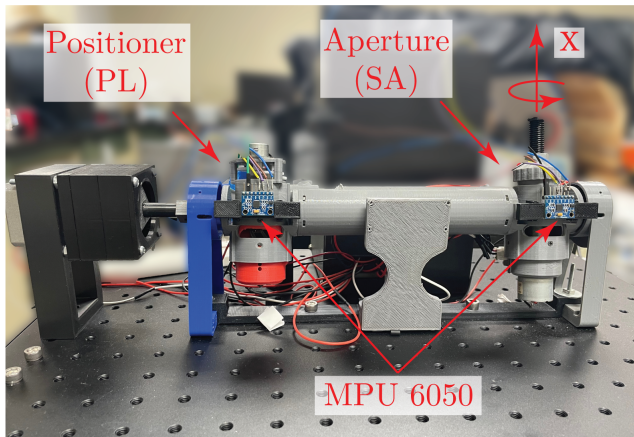


**Figure 5** MPU6050 sensor placement on Positioning Laser (PL) and Scanning Aperture (SA) subsystems for vibration data collection.

Prior to experimental data collection, the MPU6050 sensors underwent a standard calibration process to ensure accurate measurement of vibration data. This calibration involved placing each sensor on a flat, vibration-free surface to record baseline (zero-motion) readings, which were then used to offset sensor biases. Subsequently, the sensors were rotated and positioned along known orientations (X, Y, and Z axes) to verify and adjust measurement accuracy for angular velocity and linear acceleration. After this calibration, the sensors were securely mounted on the TVS subsystems to avoid measurement deviations caused by relative motion or misalignment during experiments.

### Design of Experiment A

To accurately measure mechanical vibrations at critical points of the TVS laser scanning prototype, two MPU6050 modules were utilized. These modules measure linear acceleration and angular velocity in three dimensions: X, Y, and Z. Each module, equipped with an accelerometer and a gyroscope, was strategically placed at key locations of the prototype: the PL and the SA (see Figure 5). These locations were selected because they contain optoelectronic elements that are susceptible to mechanical vibrations. Care was taken to ensure that both modules were precisely aligned along the X-axis, which is the primary axis of rotation for the scanning aperture's DC motor. The results, summarized in Fig. 6, provide a foundation for further refinement of the control system.

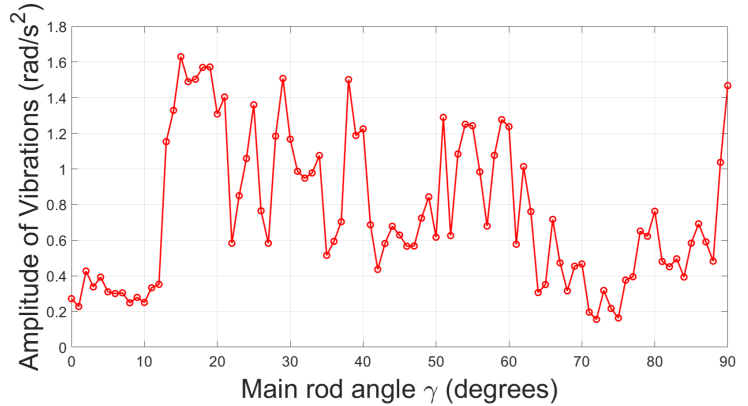


**Figure 6** Maximum amplitudes of vibration data (angular acceleration around the X-axis) measured during rotational motion at various angular positions of the main rod of TVS prototype.

Once the sensors were calibrated, they were placed in a fixed position, as shown in Figure 5, from which data collection began. For each angular position, 3000 data points (1000 per axis) were captured over a period of 2 minutes. This procedure was repeated, incrementally increasing the angular position by one degree at a time, until reaching a final position of 90 degrees. By analyzing the data across different angular positions, the dominant frequencies of the vibrations for the SA subsystem were obtained for each rotational speed (RPS) value. These results are summarized in Table 2. Deviations from this trend, such as those around 30 Hz, were not considered in the model, as they likely represent external resonances or higher-order system dynamics beyond the scope of this study.

**Table 2** Dominant Frequencies and Corresponding Spectral Amplitudes Captured from Vibration Measurements at Different Rotational Speeds (RPS) for the Scanning Aperture Subsystem

RPS (Hz)	Dominant Frequency (Hz)	Spectral Amplitude (rad/s <sup>2</sup> )
15	15.4667	0.0234
20	19.8667	0.0851
25	24.0163	0.2368

### Design of Experiment B

In the second experiment, the angles  $\gamma$  and  $\varphi$  were varied within the FOV (as shown in Figures 7, 8 and 9) to analyze their effect on the spatial components, evaluating the system's sensitivity and how vibrations impact the stability and precision of the trajectories. This analysis aims to identify mechanical error sources and their interaction with angular parameters. Specifically, the following angular values were used as reference: For  $\gamma$ , the values were  $\gamma_1 = 15^\circ$ ,  $\gamma_0 = 0^\circ$ , and  $\gamma_2 = -15^\circ$ . For  $\varphi$ , the values were  $\varphi_1 = 40^\circ$ ,  $\varphi_0 = 60^\circ$ , and  $\varphi_2 = 80^\circ$ . These values facilitated a systematic evaluation of the interaction between angular parameters and the mechanical behavior of the system under varying conditions.

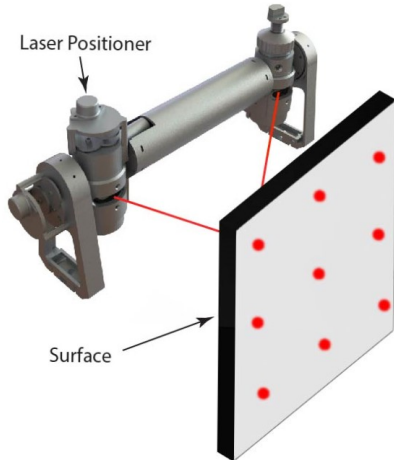


**Figure 7** Laser scanning denoting selected targets.

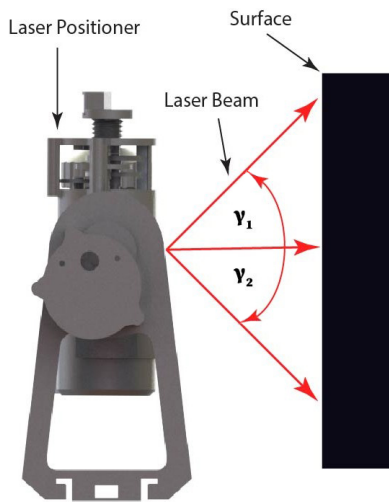


**Figure 8** Side view of the TVS prototype denoting selected  $\gamma$  values.

The heat map in Figure 10 illustrates (by color intensity) the maximum vibration amplitude obtained ( $\text{rad/s}^2$ ) observed in each test for the PL and SA subsystems under varying scanning velocities (RPS) and main inclinations of the rod ( $\gamma$ ) denoting as red the highest value. The rows represent different values of  $\gamma$  ( $-15^\circ, 0^\circ, 15^\circ$ ), while the columns distinguish between PL and SA subsystems at scanning velocities of 15, 20, and 25 RPS. Higher

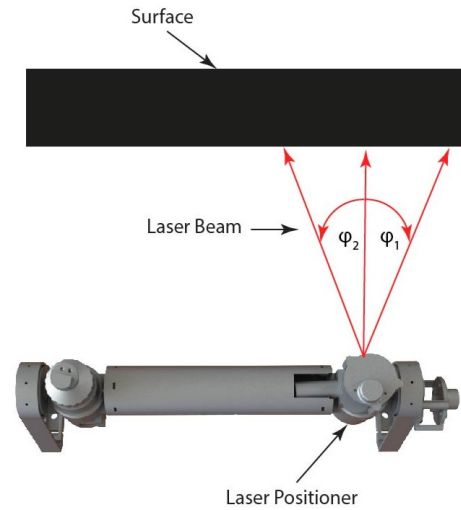


**Figure 9** Top view of the TVS prototype denoting selected  $\varphi$  values.

amplitudes, marked in warmer colors, indicate stronger vibration effects, which can be correlated with increased inclination or scanning speed. Based on the experimental results, the maximum disturbance amplitude captured was  $1.65 \text{ rad/s}^2$ , observed under the highest scanning velocity and inclination conditions. These findings highlight the sensitivity of the system to mechanical vibrations under specific operational conditions.

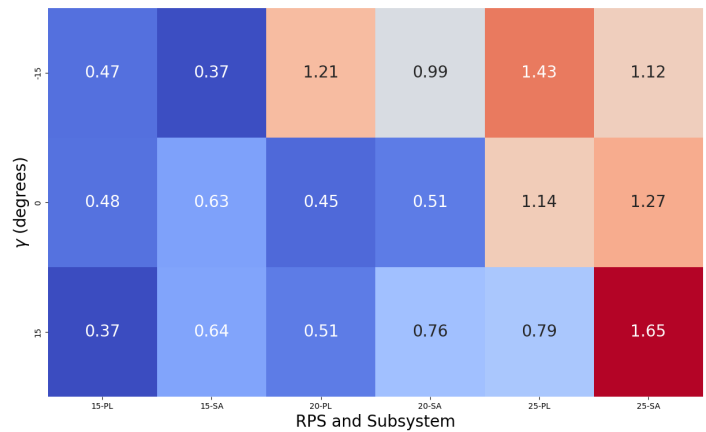


**Figure 10** Heatmap depicting maximum vibration amplitudes (in  $\text{rad/s}^2$ ) for PL and SA subsystems, varying main-rod inclination ( $\gamma$ ) and scanning velocities (15, 20, 25 RPS). Red indicates higher vibration levels.

By comparing the obtained spectral amplitudes (Table 2) with the maximum amplitudes obtained from the perturbations captured by the sensor (summarized in Figures 10 and 11), it is evident that the spectral amplitudes are significantly smaller. Additionally, as shown in Figure 6, it is evident that, regardless of the value of  $\gamma$ , there is no way to establish a linear or deterministic model for the mechanical vibrations.

This observation suggests that the deterministic component of the vibrational model is negligible, further supporting the validity of the proposed stochastic model for the chaotic mechanical perturbations, as defined in Equation (12). Consequently, this justifies

■ **Table 3** Estimated Parameters for SA

Exp	$J$ Kg · m <sup>2</sup>	$k_v$ N·m·s rad	$\tau_c$ N · m	$\tau_s$ N · m	$\sigma_0$ N·m rad	$\sigma_1$ N·m·s rad	$v_o$ rad/s
Exp1	$3.084 \times 10^{-5}$	$1.1881 \times 10^{-2}$	$1.7257 \times 10^{-7}$	$3.6951 \times 10^{-4}$	$4.2880 \times 10^{-4}$	$7.7965 \times 10^{-6}$	0.0290
Exp2	$6.286 \times 10^{-5}$	$1.1831 \times 10^{-2}$	$1.6614 \times 10^{-7}$	$3.8451 \times 10^{-4}$	$4.0718 \times 10^{-4}$	$8.1163 \times 10^{-6}$	0.0284
Exp3	$7.561 \times 10^{-5}$	$1.2627 \times 10^{-2}$	$1.7172 \times 10^{-7}$	$3.6763 \times 10^{-4}$	$4.2464 \times 10^{-4}$	$8.0763 \times 10^{-6}$	0.0293
Exp4	$6.298 \times 10^{-5}$	$1.9373 \times 10^{-2}$	$1.6520 \times 10^{-7}$	$3.8187 \times 10^{-4}$	$4.0889 \times 10^{-4}$	$8.1963 \times 10^{-6}$	0.0285
Exp5	$6.123 \times 10^{-5}$	$1.9153 \times 10^{-2}$	$1.7274 \times 10^{-7}$	$3.7138 \times 10^{-4}$	$4.2131 \times 10^{-4}$	$7.8207 \times 10^{-6}$	0.0291
Exp6	$6.378 \times 10^{-5}$	$1.9080 \times 10^{-2}$	$1.6632 \times 10^{-7}$	$3.8379 \times 10^{-4}$	$4.1005 \times 10^{-4}$	$8.1402 \times 10^{-6}$	0.0284
Exp7	$6.727 \times 10^{-5}$	$2.7189 \times 10^{-2}$	$1.7222 \times 10^{-7}$	$3.6650 \times 10^{-4}$	$4.2671 \times 10^{-4}$	$8.1963 \times 10^{-6}$	0.0292
Exp8	$6.755 \times 10^{-5}$	$2.6774 \times 10^{-2}$	$1.6580 \times 10^{-7}$	$3.8063 \times 10^{-4}$	$4.0718 \times 10^{-4}$	$8.1963 \times 10^{-6}$	0.0283
Exp9	$6.775 \times 10^{-5}$	$2.7780 \times 10^{-2}$	$1.7292 \times 10^{-7}$	$3.6837 \times 10^{-4}$	$4.2255 \times 10^{-4}$	$7.8765 \times 10^{-6}$	0.0293

the exclusion of any deterministic term in the formulation of  $\Delta_v(t)$ .

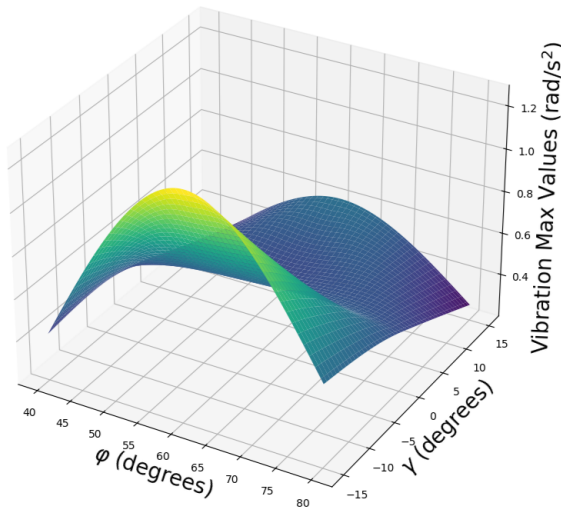


**Figure 11** 3D Surface representation of maximum vibration amplitudes measured in SA under different conditions of laser positioning.

The selection of experimental parameters was constrained by system limitations. Higher scanning velocities increased outliers in sensor data, reducing reliability, while lower velocities were impractical for real-time navigation and laser scanning. The chosen values balance accuracy and feasibility, ensuring robust data acquisition. Similarly, angles  $\gamma$  and  $\phi$  were set based on field-of-view constraints, detailed in (Alaniz-Plata *et al.* 2025; Sepulveda-Valdez *et al.* 2024).

### Characterization and Parameter Estimation

Parameter estimation refers to the process of identifying the dynamical system's constants by minimizing the discrepancy between experimental data and the mathematical model's predictions. Depending on the nature of the parameters and the available data, this can involve direct experimental measurement, statistical analysis, or optimization algorithms. The overall approach typically consists of three main steps:

1. **Mathematical Modeling:** The system's dynamics are described using mathematical equations that characterize the behavior of the system.
2. **Experimentation:** Measurements are obtained from the real system to capture its dynamic behavior.
3. **Data Preparation:** The collected data are refined to match the duration of the simulation time and ensure that the experiment starts at  $t = 0$ .

According to the recorded experimental data, the stochastic noise parameter  $\sigma_v$  can be parameterized using the maximum (0.8069 rad/s<sup>2</sup>), average (0.3381 rad/s<sup>2</sup>), or minimum (0.0838 rad/s<sup>2</sup>) amplitudes of the observed perturbations. These alternatives provide flexibility for modeling  $\Delta_v(t)$ , where the maximum ensures an upper-bound estimation, the average represents typical amplitudes, and the minimum reflects an optimistic scenario. It is important to note that this parameterization of chaotic vibrations was based solely on experimental data without relying on an optimization algorithm.

In this study, the parameters associated with frictional effects were estimated using MATLAB's Bounded Design Optimization Tool. Similar to (Núñez-López *et al.* 2023), MATLAB's Parameter Estimation app from the Simulink Design Optimization toolbox was employed, using a bounded nonlinear least-squares algorithm to estimate parameters within predefined limits. Parameter estimation was completed once the optimization tool minimized the error between the model simulation results and the experimental observations (Thenozhi *et al.* 2022).

After conducting a series of experiments at the nine reference points highlighted in Figure 7, the corresponding parameters were estimated and are presented in Table 3.

Throughout the nine experiments, the estimated values of  $k_M$  remained consistently close to  $8.526 \times 10^{-3} \text{ N} \cdot \text{m}/\text{A}$ , demonstrating a stable torque constant for the motor under varying conditions. Notice that the authors consider numerically  $k_M = k_b$  due to the fact that the motor model assumes no electromagnetic energy losses and that SI units are used ( $\text{V} \cdot \text{s}/\text{rad}$  for  $k_b$ ). Furthermore, the parameters measured directly for the tested motor were the resistance of the DC armature  $R = 11.36 \Omega$  and the inductance of the armature  $L = 1.332 \times 10^{-3} \text{ H}$ . These values are consistent with the motor's electrical dynamics, which were validated during the parameter estimation process.

### CONTROL STRATEGY TO MITIGATE MODELED NONLINEAR EFFECTS

To mitigate the modeled nonlinear effects, the control input  $u(t)$  is computed using a robust nonlinear control law derived from Lyapunov stability criteria. This control law, explicitly integrated into Equation (11) of the system model, is designed to directly compensate the nonlinear friction torque  $\tau_f(t)$  (modeled by the LuGre model) and the stochastic perturbations  $\Delta v(t)$ . The robust gain  $G_r$  used in the control formulation was specifically selected based on the maximum observed friction and vibration values, ensuring that the controller robustly counteracts these disturbances. Achieving stability of the actuator velocity is crucial for accurately determining the incidence angle  $\beta$ , necessary for the precise calculation of 3D coordinates using equations (1), (2), and (3).

#### Control Law Formulation

To perform a robust nonlinear proportional derivative control, the proposed control law to decrease the negative effect of vibrations is defined as follows:

$$u = -G_p \tanh(\epsilon) - G_d \tanh(\dot{\epsilon}) - G_r \tanh(G_0 \epsilon) \quad (18)$$

where:

- $u$  is the control input.
- $\epsilon$  and  $\dot{\epsilon}$  are the tracking error and its time derivative, respectively.
- $G_p, G_d, G_r$  are the positive proportional, derivative, and robust gains, respectively.
- $G_0$  is a sharpness factor enhancing the robustness aspect by strengthening the response as the error  $\epsilon$  increases.

Mathematically,  $\tanh(x)$  saturates to  $\pm 1$  as  $x \rightarrow \pm\infty$ , which means:

$$|u| \leq G_p + G_d + G_r \quad (19)$$

ensuring that the maximum possible control input magnitude does not exceed the sum of the gains.

In this formulation, the positioning error  $\epsilon$  is defined as:

$$\epsilon = \phi_r - \phi \quad (20)$$

where  $\phi$  is the actual position, and  $\phi_r$  is a positive constant reference angular position for the DC motor's shaft of the SA.

As depicted in Figure 12, the reference angle  $\phi_r$  is compared with the actual angle  $\phi$ , generating an error  $\epsilon$ . The robust controller then computes the control input  $u$  to regulate the scanning aperture's velocity by counteracting the nonlinear friction torque  $\tau_f(t)$

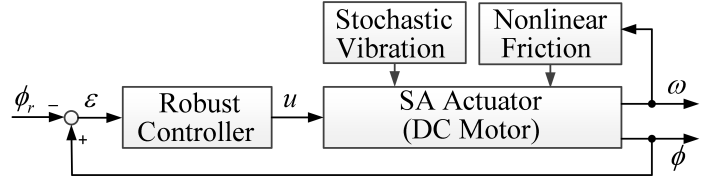


**Figure 12** Block diagram illustrating the robust control strategy integrated into the system's model.

and the stochastic vibration term  $\Delta v(t)$ . This approach ensures that both position and velocity remain bounded, thereby guaranteeing stable operation of the scanning aperture for accurate incidence angle determination.

#### Lyapunov Stability Analysis

Upon substituting the proposed control law (18) into the motion system's dynamic equation (10), the closed-loop mechanical dynamics are described by:

$$J\dot{\omega} = -\tilde{k}_u G_p \tanh(\epsilon) - \tilde{k}_u G_d \tanh(\dot{\epsilon}) - \tilde{k}_u G_r \tanh(G_0 \epsilon) - k_v \omega - \tau_f - \tau_v \quad (21)$$

where  $J$  is the system inertia,  $k_v$  is the viscous damping coefficient,  $\tau_f$ , and  $\tau_v$  represent the nonlinear friction and vibration torques, respectively. Finally,  $\tilde{k}_u$  (torque-to-control gain) directly scales the generated torque, simplifying the analysis due to the significantly smaller electrical time constant compared to the mechanical time constant, as observed in similar systems according to the literature (Ogata 2020; Kuczmann 2024).

The proposed control given by (18) ensures global asymptotic positioning stability provided the control gains are chosen to satisfy the constraint given by (19) and the following sufficient conditions:

$$G_p > \frac{G_d}{2} \quad (22)$$

$$G_r \geq \frac{\tau_s + \tau_v}{\tilde{k}_u} \quad (23)$$

To facilitate subsequent analysis, a filtered positioning signal is defined as follows, similar to (Núñez-López et al. 2021) and (Zheng et al. 2019):

$$\xi = \dot{\epsilon} + \eta \tanh(\epsilon) \quad (24)$$

where  $\eta$  is an arbitrarily small positive constant that satisfies the following condition:

$$0 < \eta < \frac{k_v}{J} \quad (25)$$

The open-loop filtered error dynamics are obtained by taking the time derivative of (24):

$$\dot{\xi} = J\dot{\omega} + \eta \text{sech}^2(\epsilon) \dot{\epsilon} \quad (26)$$

where  $\text{sech}(\cdot)$  is the standard hyperbolic secant function. Multiplying both sides of (26) by  $J$  and noting that  $\ddot{\epsilon} = \dot{\omega}$  and  $\dot{\epsilon} = \omega$  for position control, the equation becomes:

$$J\dot{\xi} = J\dot{\omega} + J\eta \text{sech}^2(\epsilon) \omega \quad (27)$$

Substituting  $J\dot{\omega}$  from (21) into (27), the resulting expression is:

$$\begin{aligned}
J\dot{\omega} = & -\tilde{k}_u G_p \tanh(\epsilon) - \tilde{k}_u G_d \tanh(\dot{\epsilon}) \\
& -\tilde{k}_u G_r \tanh(G_0 \epsilon) - [k_v - J\eta \operatorname{sech}^2(\epsilon)]\omega \\
& -\tau_f - \tau_v
\end{aligned} \quad (28)$$

The stability proof proceeds using Lyapunov's direct method (Slotine *et al.* 1991). For this purpose, the Lyapunov function candidate is proposed as:

$$\begin{aligned}
V = & \frac{1}{2} \tilde{J} \dot{\zeta}^2 + \tilde{k}_u [G_p + G_r] \int_0^\epsilon \tanh(\sigma) d\sigma \\
& + \eta \int_0^\epsilon [k_v - \eta] \operatorname{sech}^2(\sigma) \tanh(\sigma) d\sigma
\end{aligned} \quad (29)$$

From the property of the standard hyperbolic secant function and the condition (25) on  $\eta$ , it has  $k_v - \eta] \operatorname{sech}^2(\sigma) \geq k_v - \eta] \geq 0$ . Together with the fact that  $\tanh(\epsilon)\epsilon \geq 0$  for all  $\epsilon$ , and  $\tanh(\epsilon)\epsilon = 0$  only for  $\epsilon = 0$  it is straightforward to verify that the integral terms are positive and/or semi-positive definite with respect to  $\epsilon$ .

Taking the time derivative of  $V$  along (29) leads to

$$\begin{aligned}
\dot{V} = & J\dot{\zeta}\dot{\zeta} + \tilde{k}_u G_p \tanh(\epsilon)\dot{\epsilon} + \tilde{k}_u G_r \tanh(\epsilon)\dot{\epsilon} \\
& + \eta [k_v - \eta] \operatorname{sech}^2(\epsilon) \tanh(\epsilon)\dot{\epsilon}
\end{aligned} \quad (30)$$

After substituting  $J\dot{\zeta}$  from (28) into (30) using the fact that  $\dot{\epsilon} = \omega_o$  for position control, recalling the fact that  $-\tau_f(\omega)\omega \leq 0$  from (15) (due to the symmetry about the origin of the model), and  $\operatorname{sech}^2(\epsilon) \leq 1$  from the property of the hyperbolic secant function, the upper bound for  $\dot{V}$  is

$$\begin{aligned}
\dot{V} \leq & -\tilde{k}_u G_d \tanh(\omega)\omega - \tilde{k}_u G_r \tanh(G_0 \epsilon)\omega - [k_v - \eta] \omega^2 \\
& -\tau_v \omega - \eta \tilde{k}_u G_p \tanh^2(\epsilon) - \eta \tilde{k}_u G_d \tanh(\omega) \tanh(\epsilon) \\
& -\eta \tilde{k}_u G_r \tanh(G_0 \epsilon) \tanh(\epsilon) - \eta \tau_f \tanh(\epsilon) \\
& -\eta \tau_v \tanh(\epsilon) + \tilde{k}_u G_r \tanh(\epsilon)\omega
\end{aligned} \quad (31)$$

From the trigonometric property of the hyperbolic tangent function, the following inequality is defined:

$$-\eta \tilde{k}_u G_d \tanh(\omega) \tanh(\epsilon) \leq \frac{\eta \tilde{k}_u G_d}{2} [\tanh^2(\omega) + \tanh^2(\epsilon)] \quad (32)$$

Using a proposed additional gain condition for  $G_0$  to assure the global asymptotic stability, leading to if  $1 \leq G_0$ , hence  $\tanh(\epsilon) \leq \tanh(G_0 \epsilon)$ , and applying the fact  $\tanh(\omega)\omega \geq \tanh^2(\omega)$  from the standard hyperbolic tangent function to (31) leads to:

$$\begin{aligned}
\dot{V} \leq & -\tilde{k}_u G_d \left[ 1 - \frac{\eta}{2} \right] \tanh^2(\omega) - [k_v - \eta] \omega^2 - \tau_v^{max} |\omega| \\
& -\eta \left[ \tilde{k}_u G_p - \frac{\eta \tilde{k}_u G_d}{2} + \tilde{k}_u G_r - \tau_s - \tau_v^{max} \right] \tanh^2(\epsilon)
\end{aligned} \quad (33)$$

where are used the inequalities (14), (17), (32) and  $|\tanh(\epsilon)| \geq \tanh^2(\epsilon)$  from the property of the hyperbolic tangent function.

By the conditions on control gains (22), (23) and (25), the final upper bound for  $\dot{V}$  can be written as

$$\dot{V} \leq -\rho_1 \tanh^2(\omega) - \rho_2 \omega^2 - \rho_3 |\omega| - \rho_4 \tanh^2(\epsilon) \quad (34)$$

where  $\rho_1, \rho_2, \rho_3$ , and  $\rho_4$  are some positive constants.

The detailed derivation demonstrates that  $\dot{V}$  is negative definite. By applying Barbalat's lemma (Slotine *et al.* 1991), the authors conclude that  $\lim_{t \rightarrow \infty} \tanh^2(\omega) = 0$ ,  $\lim_{t \rightarrow \infty} \omega^2 = 0$ ,  $\lim_{t \rightarrow \infty} |\omega| = 0$ , and  $\lim_{t \rightarrow \infty} \tanh^2(\epsilon) = 0$ , thereby ensuring global asymptotic stability for any initial states  $(\phi(0), \omega(0))$ .

## RESULTS AND DISCUSSION

The purpose of this analysis is to evaluate the effect of mechanical vibrations on the precision of the measured coordinates. Vibrational disturbances can introduce variability in the system, potentially affecting the stability of the scanning process and the accuracy of the spatial measurements. By examining the standard deviations, the authors aim to quantify how the vibrational effects propagate across the different coordinate components.

Figure 13 depicts the open-loop velocity response under multiple operating conditions. The signal exhibits irregular, abrupt, non-periodic fluctuations that suggest a complex, chaotic behavior induced by the synergy of nonlinear friction (modeled by the LuGre approach) and random perturbations, which are represented as stochastic mechanical vibrations in this study. Such chaotic mechanical dynamics negatively affect the system's accuracy because the scanning aperture must maintain as stable a velocity as possible to accurately determine the incidence angle  $\beta$ , which is essential for calculating the 3D coordinates of objects within the field of view using equations (1), (2) and (3). Stochastic angular velocity fluctuations demonstrate a complex dynamic behavior that requires robust control to mitigate performance degradation.

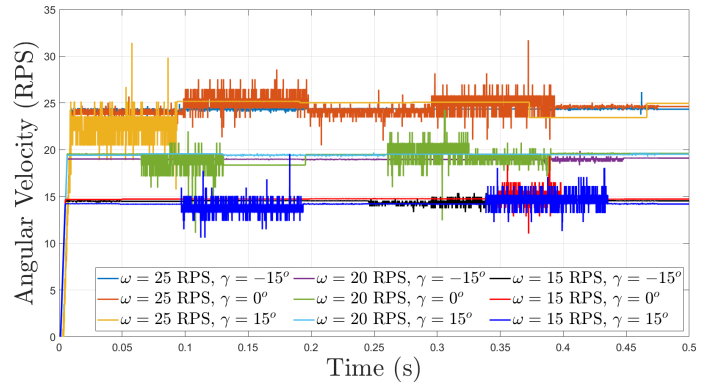


**Figure 13** Angular velocity in RPS of the actuator versus time under various operating conditions.

Table 4 presents the experimental uncertainties  $\sigma_x$ ,  $\sigma_y$ , and  $\sigma_z$  for the coordinates  $x$ ,  $y$ , and  $z$ , respectively, under different inclination angles  $\gamma$ . These uncertainties represent the standard deviation of the coordinate errors, derived from experimental data collected under varying vibrational conditions. From the results in Table 4, it is observed that  $\sigma_x$  and  $\sigma_z$  show a slight decrease as the inclination  $\gamma$  changes from  $-15^\circ$  to  $15^\circ$ . Specifically,  $\sigma_x$  decreases from  $2.88056mm$  to  $2.58106mm$ , while  $\sigma_z$  decreases from  $2.00934mm$  to  $1.71697mm$ . In contrast,  $\sigma_y$  remains consistently smaller in magnitude, with values close to  $0.7mm$ , except for a notable reduction to  $1.6 \times 10^{-2}mm$  when  $\gamma = 0^\circ$ . As previously established graphically, a numeric relation exists between inclination and vibration characteristics (as shown in Figure 11). This allows the conclusion of the empirical analysis of vibration influence on the measurement uncertainty in a particular case of the presented laser scanner.

These findings suggest that the  $x$ - and  $z$ -components are moderately affected by changes in inclination, while the  $y$ -component exhibits a minimal sensitivity to the vibrational disturbances.

■ **Table 4** Average Experimental Uncertainty (in mm)

$\gamma$ (Inclination)	$\sigma_x$ (mm)	$\sigma_y$ (mm)	$\sigma_z$ (mm)
$-15^\circ$	2.88	0.77	2.01
$0^\circ$	2.68	0.016	1.82
$15^\circ$	2.58	0.69	1.72

The analysis of the proposed controller's performance was focused exclusively on the  $x$ -axis, as detailed in the Model Validation section. This axis was selected due to its primary role in the scanning aperture's rotational dynamics. The computational implementation of the robust control strategy was evaluated based on its ability to mitigate the nonlinear effects of mechanical vibrations and friction. The robust gain,  $G_r$ , was particularly chosen to ensure stability under the maximum observed vibrational and frictional disturbances, aligning the control parameters with the experimentally captured data.

To assess the controller's performance under varying gain configurations, metrics such as settling time and maximum overshoot were evaluated for each positioning cycle across a range of angular positions. The parameter ranges employed in these tests are presented in Table 5. The resulting data enabled the identification of an optimal set of control gains that minimized both settling time and overshoot while maintaining the stable operation of the scanning aperture.

■ **Table 5** Ranges of Proportional, Derivative, Robust Gains, and Reference Positions Employed during the Robust Control Law Evaluation

Parameter	Range of Values
Proportional Gain ( $G_p$ )	1.25, 3.78, 6.31
Derivative Gain ( $G_d$ )	0.5, 3.11, 8.33
Robust Gain ( $G_r$ )	16.33, 18.89, 21.44
Sharpness Factor ( $G_0$ )	10, 100, 150
Reference Positions (degrees)	5, 20, 25, 30, 35, 40, 45

The proposed nonlinear control strategy was assessed by measuring the average settling time, maximum overshoot, and final positioning accuracy across various target positions. These results were summarized in and are presented in Table 6.

In Fig. 14, the phase portrait depicts the relationship between angular position (in radians) and angular velocity (in rad/s) for distinct sets of controller gains prior to stabilization at a reference position of 5 degrees. Fig. 15 illustrates the oscillatory behavior of the system's angular position before achieving the desired reference, while Fig. 16 highlights the oscillations in angular velocity during the same interval. The black and red curves exhibit greater oscillatory behavior compared to the blue curve, underscoring

the stabilizing effect of the gain  $G_0$ . Specifically, the configuration with  $G_0 = 10$  (blue curve) achieved the smoothest response and the least overshoot, while the setup with  $G_0 = 150$  (black curve) demonstrated the most pronounced oscillations and the longest stabilization time.

■ **Table 6** Summary of Results Obtained under Varying Reference Positions for the Robust Nonlinear Controller

Ref. Position	Average Time	Settling	Average Maximum Overshoot
5	0.019139		4.95
20	0.036022		19.98
25	0.041547		24.93
30	0.044959		29.97
35	0.049019		34.92
40	0.053001		39.96
45	0.056768		45.00

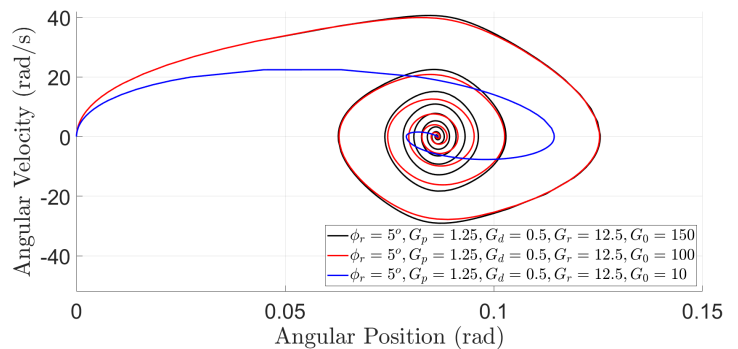


**Figure 14** Phase portrait of system's angular position and velocity for different controller constants.

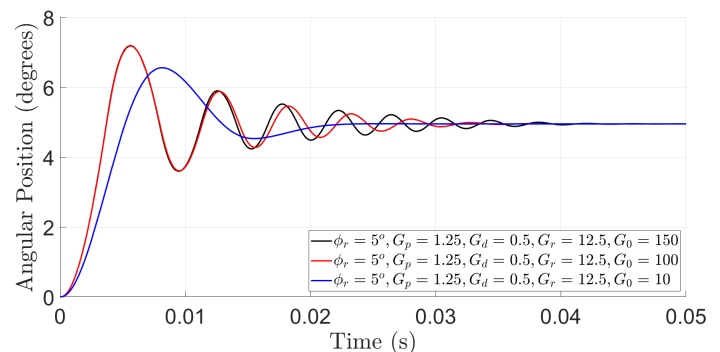


**Figure 15** System's position response for different controller constants.

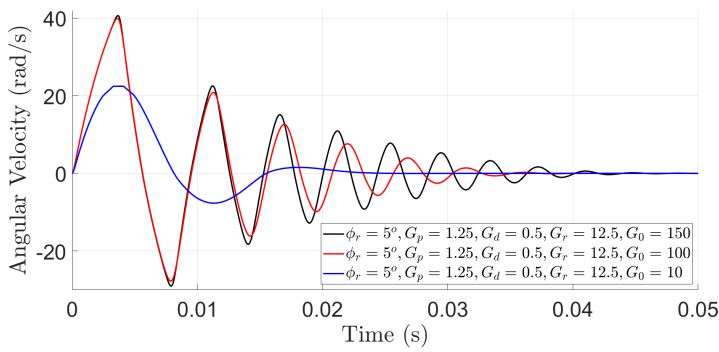


**Figure 16** System's velocity response for different controller constants.

The results highlight the effectiveness of the proposed control strategy in maintaining system stability while minimizing the settling time and maximum overshoot. By leveraging the robust gain  $G_r$  calibrated to the upper limits of the observed disturbances, the controller demonstrated the ability to ensure smooth operation even under varying dynamic conditions. These findings validate the computational implementation of the control strategy, paving the way for future physical testing and refinement. The Lyapunov stability analysis confirmed the global asymptotic stability of the system, providing theoretical guarantees for the controller's robustness under bounded disturbances.

## CONCLUSION

This work developed a physical-mathematical model to describe the mechanical vibrations and nonlinear friction effects in laser scanning systems, integrating both deterministic and stochastic terms that reflect their chaotic nature. Experimental measurements obtained using MPU6050 sensors validated the model, highlighting the significance of random perturbations and their impact on system dynamics.

The findings presented here align with prior studies on nonlinear dynamics in precision systems, particularly regarding the LuGre friction model's effectiveness in capturing nonlinear friction phenomena, as demonstrated in (Canudas de Wit *et al.* 1995; Wang *et al.* 2016; Freidovich *et al.* 2009). However, the distinctive contribution of this work lies in explicitly characterizing and incorporating the chaotic mechanical vibrations measured experimentally into a robust nonlinear control framework. The present study focused on modeling the nonlinear vibrational response of the TVS within typical operational conditions (scanning speeds below 25 RPS) to ensure data acquisition while maintaining realistic performance constraints. Chaotic behavior was explicitly confirmed experimentally through irregular velocity fluctuations at the actuator shaft, with disturbances reaching up to  $1.65 \text{ rad/s}^2$  under demanding conditions (25 RPS,  $\pm 15^\circ$  inclination).

The proposed model not only provides a tool to analyze and understand the inherent complexities of friction and vibration in mechanical systems but also opens opportunities for designing robust control strategies. In this regard, a nonlinear controller based on hyperbolic functions was implemented computationally to mitigate the effects of chaotic perturbations and ensure operational stability. After applying the proposed methodology in the computational implementation, the visualized results suggest a reduction in the negative influence of chaotic signals, leading to a more stable simulated system response. The results demonstrate

the effectiveness of this approach, showcasing its potential for high-precision system applications. Future work will aim to implement the proposed control strategy on a physical TVS system prototype, enabling the validation of simulation outcomes under real-world operating conditions.

Limitations of the present study include assumptions made in modeling vibrations as purely stochastic processes, potentially neglecting minor deterministic resonance effects that might influence system behavior. Additionally, the robust control strategy was validated through computational simulations, and its effectiveness under practical implementation constraints, such as actuator saturation or sensor noise, remains to be experimentally verified. The typical operational conditions of TVS to minimize the occurrence of outliers were studied according to previous research (Alaniz-Plata *et al.* 2025; Sepulveda-Valdez *et al.* 2024; Sergiyenko *et al.* 2024). However, further investigation is needed to analyze the effect of material properties on vibrational stability at higher speeds.

## APPENDIX

### Abbreviations and Symbols

**Table 7** Most Relevant Symbols Used in the Manuscript.

Symbol	Description
$\varphi, \beta, \gamma$	Angles in Dynamic Triangulation Method
$a$	Fixed distance between PL and SA subsystems
$R, L$	DC motor armature resistance and inductance
$J$	Moment of inertia of DC motor and SA assembly
$k_M, k_b$	DC motor torque constant and back-EMF constant
$k_v$	Viscous damping friction coefficient of DC motor
$\tau_s, \tau_c$	Static friction torque and Coulomb friction torque
$\sigma_0, \sigma_1$	LuGre friction stiffness and damping coefficients
$v_0$	Stribeck velocity threshold in friction model
$\sigma_v$	Standard deviation of experimentally measured stochastic vibration disturbance
$G_p, G_d, G_r$	Proportional, derivative, and robust control gains
$G_0$	Sharpness factor enhancing robustness of controller
$\Delta v(t)$	Stochastic perturbation due to mechanical vibrations
$dW(t)$	Increment of Wiener process
$u(t)$	Control input voltage to DC motor
$\omega(t)$	Angular velocity of DC motor shaft
$\tau_f(t)$	Nonlinear friction torque described by LuGre model
$\tau_v(t)$	Torque induced by mechanical vibrations

■ **Table 8** Most Relevant Abbreviations Used in the Manuscript.

Abbreviation	Description
TVS	Technical Vision System
PL	Positioning Laser
SA	Scanning Aperture
DOF	Degree of Freedom
FOV	Field of View
MPU6050	Inertial Measurement Unit Sensor
RPS	Revolutions per Second

### Acknowledgments

This work was supported by the Autonomous University of Baja California.

### Availability of data and material

Additional data related to this study are available from the corresponding author upon request.

### Conflicts of interest

The authors declare that there is no conflict of interest regarding the publication of this paper.

### Ethical standard

The authors have no relevant financial or non-financial interests to disclose.

## LITERATURE CITED

Al Khawaja, H., H. Alabdouli, H. Alqaydi, A. Mansour, W. Ahmed, *et al.*, 2020 Investigating the mechanical properties of 3d printed components. In *2020 Advances in Science and Engineering Technology International Conferences (ASET)*, pp. 1–7.

Alaniz-Plata, R., F. Lopez-Medina, O. Sergiyenko, W. Flores-Fuentes, J. C. Rodríguez-Quiñonez, *et al.*, 2025 Extrinsic calibration of complex machine vision system for mobile robot. *Integration* **102**: 102370.

Armstrong-Hélouvy, B., P. Dupont, and C. C. De Wit, 1994 A survey of models, analysis tools and compensation methods for the control of machines with friction. *Automatica* **30**: 1083–1138.

Atef, M., A. El-Assal, and M. Magdy, 2022 Analysis of the parameters affecting 3d printed parts for planar and nonplanar models. In *2022 6th International Conference on Robotics and Automation Sciences (ICRAS)*, pp. 224–230.

Banerjee, S., 2021 *Mathematical modeling: models, analysis and applications*. Chapman and Hall/CRC.

Canudas de Wit, C., H. Olsson, K. Astrom, and P. Lischinsky, 1995 A new model for control of systems with friction. *IEEE Transactions on Automatic Control* **40**: 419–425.

Freidovich, L., A. Robertsson, A. Shiriaev, and R. Johansson, 2009 LuGre-model-based friction compensation. *IEEE Transactions on Control Systems Technology* **18**: 194–200.

Gohar, R. and H. Rahnejat, 2012 *Fundamentals of Tribology*. London.

Kuczmann, M., 2024 Review of dc motor modeling and linear control: Theory with laboratory tests. *Electronics* **13**: 2225.

Kumičák, J., 2004 Stochastic and deterministic models of noise. In *Advanced Experimental Methods For Noise Research in Nanoscale Electronic Devices*, edited by J. Sikula and M. Levinshtein, pp. 61–68, Dordrecht, Springer Netherlands.

Kushwaha, Y. S., N. S. Hemanth, N. D. Badgayan, and S. K. Sahu, 2022 Free vibration analysis of pla based auxetic metamaterial structural composite using finite element analysis. *Materials Today: Proceedings* **56**: 1063–1067, First International Conference on Advances in Mechanical Engineering and Material Science.

Lazutkin, G. V., D. P. Davydov, L. A. Varzhitskiy, K. V. Boyarov, and T. V. Volkova, 2017 Non-linear oscillations of mechanical systems with structure damping vibration protection devices. *Procedia Engineering* **176**: 334–343.

Lindner, L., 2021 *Theoretical method to increase the speed of continuous mapping in a three-dimensional laser scanning system using servomotors control*. Editorial UABC.

Liu, X., W. Tian, J. Yu, and J. Zhao, 2021 Lidar points' bumpy distortion model, displacements and experiments. 2021 5th CAA International Conference on Vehicular Control and Intelligence, CVCI 2021 .

Marton, L. and B. Lantos, 2007 Modeling, Identification, and Compensation of Stick-Slip Friction. *IEEE Transactions on Industrial Electronics* **54**: 511–521.

Na, J., Q. Chen, and X. Ren, 2018 Chapter 1 - friction dynamics and modeling. In *Adaptive Identification and Control of Uncertain Systems with Non-smooth Dynamics*, edited by J. Na, Q. Chen, and X. Ren, Emerging Methodologies and Applications in Modelling, pp. 11–18, Academic Press.

Núñez-López, J. A., L. Lindner, O. Sergiyenko, J. C. Rodríguez-Quiñonez, W. Flores-Fuentes, *et al.*, 2021 Positioning Improvement for a Laser Scanning System using cSORPD control. In *IECON 2021 – 47th Annual Conference of the IEEE Industrial Electronics Society*, pp. 1–6, Toronto, Canada, ISSN: 2577-1647.

Núñez-López, J. A., O. Sergiyenko, R. Alaniz-Plata, C. Sepulveda-Valdez, O. M. Pérez-Landeros, *et al.*, 2023 Advances in laser positioning of machine vision system and their impact on 3d coordinates measurement. In *IECON 2023- 49th Annual Conference of the IEEE Industrial Electronics Society*, pp. 1–6.

Ogata, K., 2020 *Modern control engineering*.

Pany, C., 2023 Large amplitude free vibrations analysis of prismatic and non-prismatic different tapered cantilever beams. *Pamukkale Üniversitesi Mühendislik Bilimleri Dergisi* **29**: 370–376.

Pany, C. and G. Rao, 2002 Calculation of non-linear fundamental frequency of a cantilever beam using non-linear stiffness. *Journal of sound and vibration* **256**: 787–790.

Pany, C. and G. V. Rao, 2004 Large amplitude free vibrations of a uniform spring-hinged beam. *Journal of sound and vibration* **271**: 1163–1169.

Popov, V. L. *et al.*, 2010 *Contact mechanics and friction*. Springer.

Selivanov, A. and E. Fridman, 2023 Finite-dimensional boundary control of a wave equation with viscous friction and boundary measurements. *IEEE Transactions on Automatic Control* .

Sepulveda-Valdez, C., O. Sergiyenko, V. Tyrsa, P. Mercorelli, J. C. Rodríguez-Quiñonez, *et al.*, 2024 Mathematical modeling for robot 3d laser scanning in complete darkness environments to advance pipeline inspection. *Mathematics* **12**.

Sergiyenko, O., R. Alaniz-Plata, W. Flores-Fuentes, J. C. Rodríguez-Quiñonez, J. E. Miranda-Vega, *et al.*, 2024 Multi-view 3d data fusion and patching to reduce shannon entropy in robotic vision. *Optics and Lasers in Engineering* **177**: 108132.

Sergiyenko, O., W. Flores-Fuentes, and P. Mercorelli, 2020 *Machine vision and navigation*. Springer.

- Slotine, J.-J. E., W. Li, *et al.*, 1991 *Applied nonlinear control*, volume 199. Prentice hall Englewood Cliffs, NJ.
- Thenozhi, S., A. C. Sánchez, and J. Rodríguez-Reséndiz, 2022 A Contraction Theory-Based Tracking Control Design With Friction Identification and Compensation. *IEEE Transactions on Industrial Electronics* **69**: 6111–6120.
- Wang, X., S. Lin, and S. Wang, 2016 Dynamic friction parameter identification method with lugre model for direct-drive rotary torque motor. *Mathematical Problems in Engineering* **2016**: 6929457.
- Zhao, Q. L., Y. X. Hao, and J. H. Wang, 2010 An application of chaos for vibration control. 2010 International Conference on Mechanic Automation and Control Engineering, MACE2010 pp. 267–270.
- Zheng, C., Y. Su, and P. Mercorelli, 2019 Faster Positioning of 1-DOF Mechanical Systems With Friction and Actuator Saturation. *Journal of Dynamic Systems, Measurement, and Control* **141**.

**How to cite this article:** Núñez-López, J. A., Meza-García, D., Sergiyenko, O., Tyrsa, V., Rodríguez-Quiñonez, J. C., Flores-Fuentes, W., Lopez-Medina, F., Sepulveda-Valdez, C., Villa-Manriquez, J. F., Andrade-Collazo, H., Burnaev, E., Illarionova, S., Cáceres- Hernández, D., and Alaniz-Plata, R. Modeling and Analysis of Nonlinear Chaotic Mechanical Dynamics in Laser Scanning Systems. *Chaos Theory and Applications*, 7(2), 125-137, 2025.

**Licensing Policy:** The published articles in CHTA are licensed under a [Creative Commons Attribution-NonCommercial 4.0 International License](https://creativecommons.org/licenses/by-nc/4.0/).

